Meteotsunamis in Japan Associated with the Tonga Eruption in January 2022

Ryuho Kataoka[1, 2, 3], Stephen D. Winn[3, 4], and Emile Touber[3, 4]
[1]*National Institute of Polar Research*, *Tachikawa*, *Tokyo*, *Japan*
[2]*SOKENDAI*, *The Graduate University for Advanced Studies*, *Hayama*, *Kanagawa*, *Japan*
[3]*Okinawa Institute of Science and Technology Graduate University*, *Onna*, *Okinawa*, *Japan*
[4]*Department of Mechanical Engineering*, *Imperial College London*, *London*, *UK*

Abstract

Large-amplitude meteotsunamis were observed in many areas in Japan, following the arrival of barometric Lamb waves emitted by an underwater volcanic eruption of Hunga Tonga-Hunga Ha'apai in January 2022. We modeled the power spectra of the tidal level data obtained from 12 tide stations of the Geospatial Information Authority of Japan, based on a method of transfer function which converts the barometric pressure pulse spectra into the meteotsunami spectra. The obtained transfer functions are similar at 12 stations. The pressure pulse spectra are obtained from the ensemble average of ~1500 Soratena weather sensors of Weathernews Inc. distributed over Japan. The observed meteotsunami spectra can be characterized by the enhanced seiche eigenmodes at each station excited by the mesoscale pressure pulse within the amplitude error of 50%, which contributes for accumulating the necessary knowledge to understand the potential dangers in various different areas over Japan.

(**Citation**: Kataoka, R., S. D. Winn, and E. Touber, 2022: Meteotsunamis in Japan associated with the Tonga Eruption in January 2022. *SOLA*, **18**, 116−121, doi:10.2151/sola.2022-019.)

1. Introduction

On 15 January 2022, at ~0400 UT, an underwater volcanic eruption of Hunga Tonga-Hunga Ha'apai at 20.54 S and 175.39 W produced a barometric pressure pulse, globally spreading out in concentric circles from the volcano (Fig. 1, Supplement 1), circling the Earth for at least two days. The pressure pulse is called an atmospheric Lamb wave, which is generated by the expansion of the air around the volcano due to the heat of the eruption. Lamb waves travel at ~310 m/s, slightly slower than the sound speed at ground level, and are characterized by weak attenuation over long distances (Nishida et al. 2014).

When the first wave front passed through Japan, a pressure pulse of ~2 hPa was observed at ~1100 UT (1900−2000 JST), and immediately after that, a large disturbance of the tidal level was observed over a wide area, especially along the Pacific coast of Japan, including the largest amplitude of ~1.2 m at Amami station (https://www.jma.go.jp/jma/press/2201/16a/202201160200.html). This phenomenon is known as a meteorological tsunami or meteotsunami. In Japan it has been known as the Abiki phenomenon in Nagasaki Bay (Hibiya and Kajiura 1982), and also reported on other west coasts of Japan. A similar pressure pulse and meteotsunami have occurred in the past during the eruption of Krakatoa volcano in Indonesia in 1883 (Harkrider and Press 1962).

The Japan Meteorological Agency (JMA), which had predicted in the evening that the Tonga eruption would have no impact in Japan, was surprised by the meteotsunami, which started a few hours earlier than the predicted arrival time of any possible tsunami. JMA then issued tsunami warnings in many areas at around midnight when the meteotsunami amplitude peaked. The warning lasted for more than a half day and was terminated at 2:00 p.m. JST (https://www.jma.go.jp/jma/press/2201/16b/202201161415.html). In order to mitigate the confusion and possible damage caused by similar phenomena in the future, an overview of the basic characteristics of the meteotsunamis observed in various parts of Japan would be useful.

Meteotsunamis are amplified due to the combination of atmospheric pressure and oceanic resonance at multiple stages, such as Proudman, shelf, and harbor effects (Proudman 1929; Hibiya and Kajiura 1982; Monserrat et al. 2006). Among those known effects, we particularly focus on the local harbor resonance working at the last stage. As for the power spectrum analysis method, to reconstruct the transfer function which converts the barometric spectra into meteotsunami spectra, we followed Monserrat et al. (1998).

The purpose of this study is to examine whether the power spectrum of meteotsunamis observed over a wide area of Japan can be modeled by the transfer function by inputting mesoscale power spectrum of the atmospheric pressure pulse, based on the localized resonance spectrum of seiches specific to each region.

2. Data and method of analysis

We use the 30 s values of tidal level data published realtime by the Geospatial Information Authority of Japan (GSI) (https://www.gsi.go.jp/kanshi/tide_furnish_e.html). The tidal level resolution is mm. Twelve stations out of 25 GSI tide stations are facing the Pacific Ocean (Fig. 2), and clearly respond to the pressure pulses.

As a pre-processing step for spectral analysis, only the high-frequency components were extracted by subtracting the 60 min moving average values for all data. To estimate the background seiche spectrum S_b at each location, the ensemble average was adopted for a total of 47 power spectra, which were shifted by 2 hours using a 4-hour window, using 4-day data preceding the event starting at 0000 UT on 11 January 2022. The meteotsunami power spectra S_{obs} were obtained for the 24-hour time periods; the first pressure pulse roughly occurred from ~1100 UT on 15 January, and the second pressure pulse occurred from ~0000 UT on 17 January. The second meteotsunami event is relatively weak, and an example from Okinawa station is shown in Fig. 3. Some areas react more or less than others during that interval.

Taking the great circle distance from the volcano to each of the tide monitoring stations, the arrival times from the explosion time are estimated for the first pressure pulse (the first grey lines in Fig. 3, assuming v = 310 m/s), the tsunami (blue lines, based on the characteristic gravitational-wave speed using the mean bathymetry along that great circle line), the inverse pressure pulse (the second grey lines) and a second passage of the pressure pulse (the third grey lines).

For the pressure pulse analysis, we also utilize the 1 min barometric pressure data of ~3000 Soratena stations distributed over Japan, as provided by Weathernews Inc. The resolution is 0.1 hPa, and the example data is shown in Fig. 3. For the pressure pulse time intervals, gapless data are available for ~1500 stations. As a pre-processing step for consistent spectral analysis, the barometric pressure data were linearly interpolated to double the number of data points, and only the high-frequency components were extracted by subtracting the 60 min moving average values.

Corresponding author: Ryuho Kataoka, National Institute of Polar Research, 10-3 Midori-cho, Tachikawa 190-8518, Japan. E-mail: kataoka.ryuho@nipr.ac.jp.

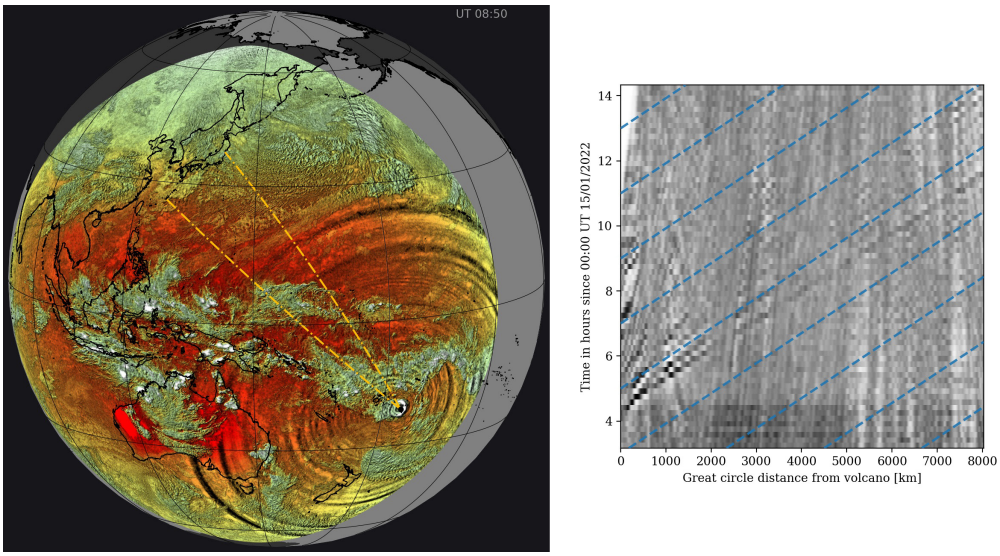

Fig. 1. (a) The color and cloud shading are based on band 8 which is infrared centered around 6.2 um, the Lamb wave is shown using time-derivative estimates on band 8, and smoothed using a Laplacian operator applied in longitude-latitude space. The orange dashed lines indicate the straight path from the volcano to the most extreme in latitude stations used in this study. See Supplement 1 (Movie A) for the movie. (b) Distance-time diagram for the Laplacian-filtered signal along the great circle path that joins the volcano and Okinawa, using Himawari-8 data. Diagonal dashed blue sloped lines of v = 310m/s for reference.

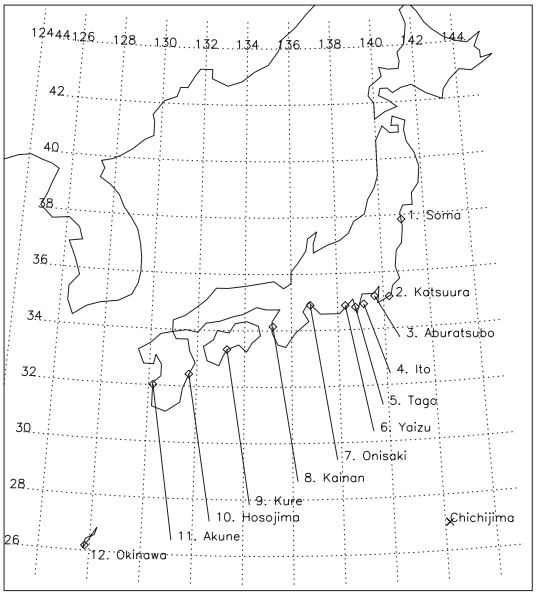

Fig. 2. Map of 12 tide stations used in this study.

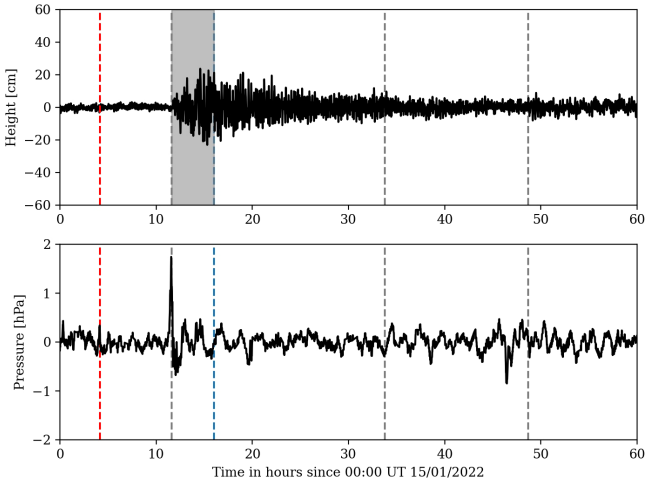

Fig. 3. Example of high-pass filtered time series of (top) tidal level and (bottom) barometric pressure from Okinawa. The red line is the explosion time, the grey lines are the pressure pulse timings and the blue line the would-be tsunami arrival time. The grey coloring indicates the time during which the pressure pulse has arrived but not the would-be tsunami.

As shown in Fig. 4, the propagating coherent pressure pulses can be clearly visualized by the Soratena weather stations, taking the angular distance of each station from the Tonga eruption. The phase speed of the first Lamb wave is estimated to be ~300 m/s with the dominant wavelength of 500−600 km, which gives the basic temporal variation at 15−20 min. The estimated propagation speed over Japan is slightly slower than the global average as seen in Himawari-8 (Fig. 1), although the small difference in the phase speed does not affect the spectral analysis of this study. More detailed analysis of the Lamb wave fronts is beyond the scope of this study.

We applied our spectral analysis for the first and the returning pressure pulses (Figs. 4a and 4c) and omitted the inverse propagation event (Fig. 4b). The barometric pressure spectra P are obtained for 4-hour time interval for the first and second events, and ensemble averaging was performed at gapless ~1500 locations (Fig. 5a). The onshore pressure data can be used in this analysis because the atmospheric wave is coherent over a large region, as we can confirm that near open-sea spectra at Chichijima Island (27.01°N, 142.19°E) are consistent (Fig. 5a), although the noise from the single station is large because of no ensemble averaging, especially for the small-amplitude event 2.

The transfer function T converts from the pressure spectrum P to the meteorological tsunami spectrum S_{obs}, which is obtained by the following equation (Monserrat et al. 1998):

$$T(\omega) = \left(\frac{S_{obs}(\omega)}{S_b(\omega)} - 1 \right) \frac{E_b(\omega)}{P(\omega)}, \quad (1)$$

where S_b and S_{obs} are the power spectra of background seiche and the observed meteotsunami. E_b is the background ocean spectrum,

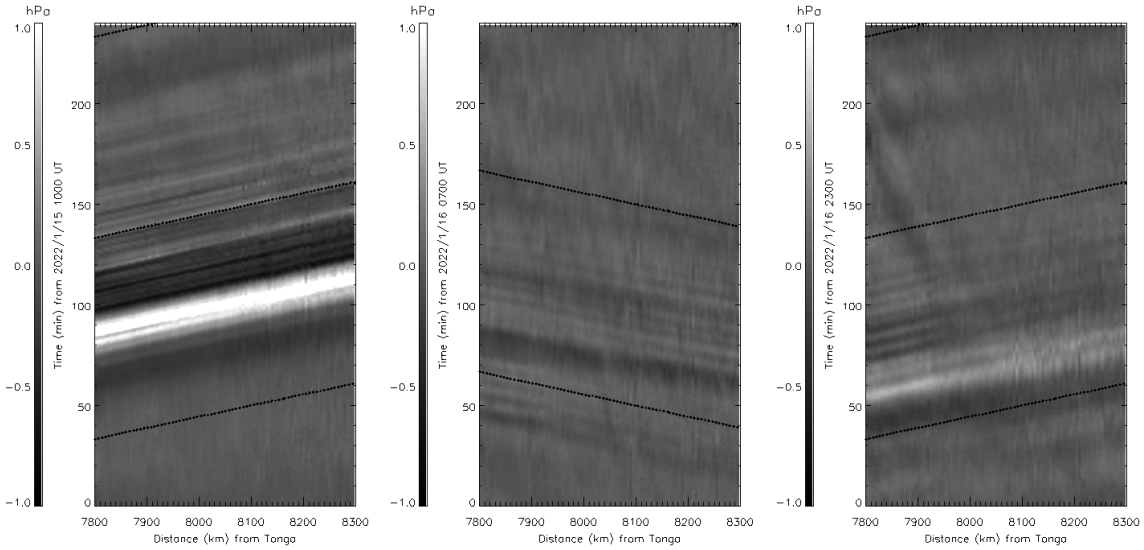

Fig. 4. Propagating pressure pulses for (a) the first wave at t = 10−14 h, (b) inverse propagation wave at t = 31−35 h, and (c) the second returning wave at t = 47−51 h. Diagonal dashed sloped lines of v = 300 m/s are also shown for reference.

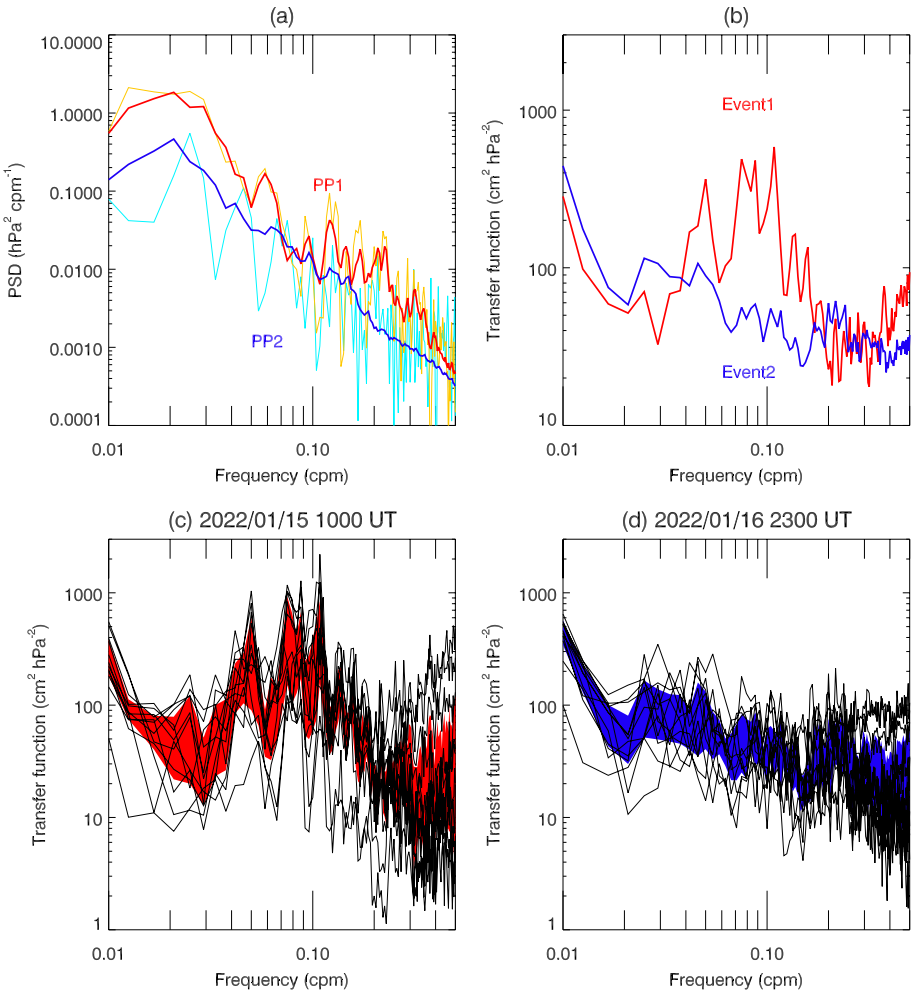

Fig. 5. (a) Power spectral density of pressure pulse event 1 (red) and event 2 (blue). The spectra from Chichijima Island are also shown by orange and sky-blue; (b) averaged transfer functions for events 1 and 2; (c) all 12 transfer functions for event 1 with the shaded area enclosing the upper and lower quartiles (d) all 12 transfer functions for event 2 with the shaded area enclosing the upper and lower quartiles.

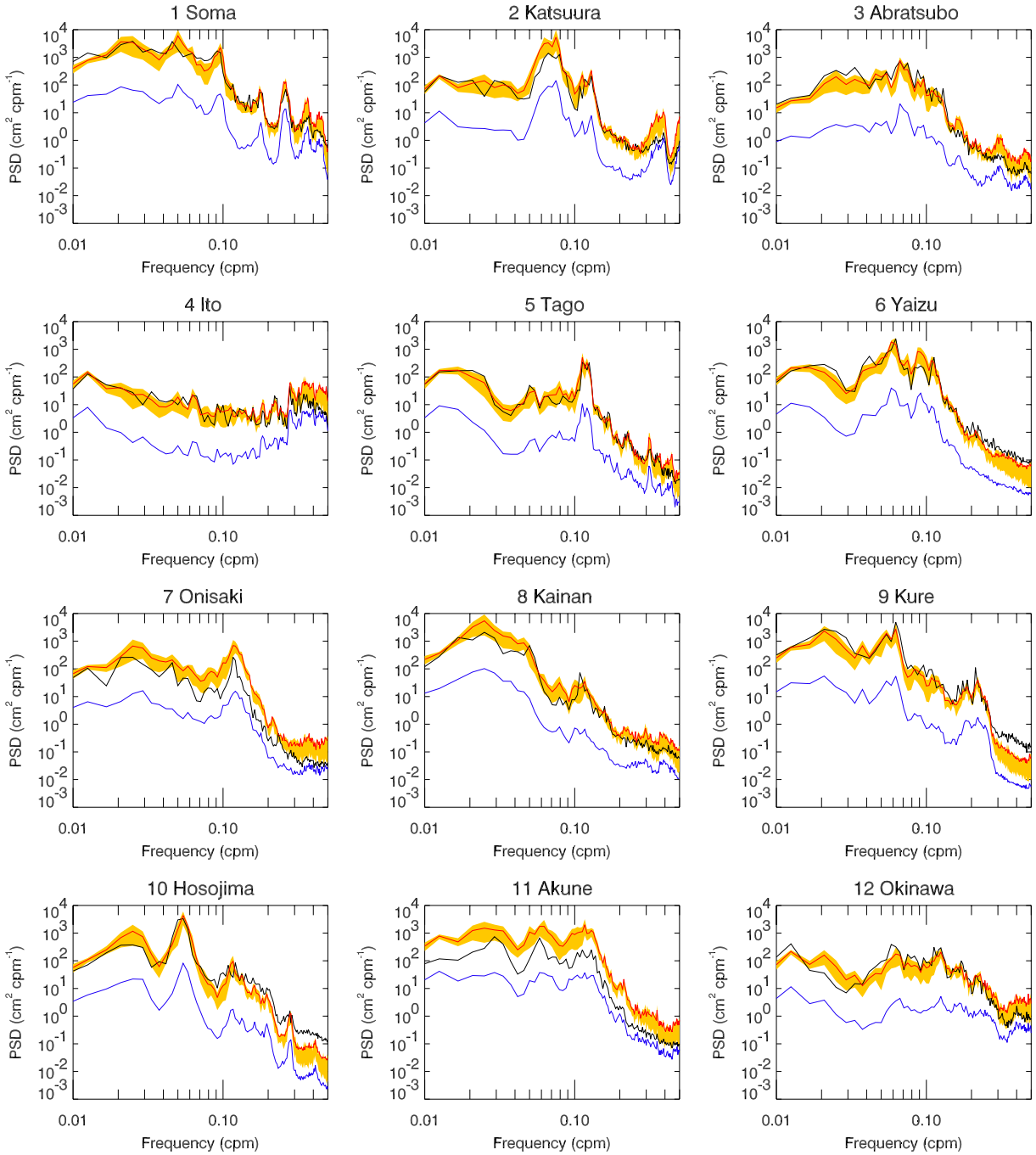

Fig. 6. Observed meteotsunami spectra (black), background seiche spectra (blue), and model spectra (red), with shaded area enclosing the upper and lower quartiles, of the first meteotsunami event for the 24-hour time interval from 1000 UT on 15 January 2022.

which is virtually universal (Kulikov et al. 1983) and can be described with a constant A by $E_b(\omega) = A\omega^{-2}$. We estimate the averaged transfer function T_{ave} by averaging all of the transfer functions obtained from 12 stations, separately for the first and second events. The averaged transfer functions are shown in Fig. 5, where A is assumed to be 10^{-3} cm^2 cpm (Rabinovich 1997). To check if the transfer functions of 12 stations are similar to some extent, all of the transfer functions are shown with the upper and lower quartiles in Figs. 5c and 5d. The possible cause of the difference between the average transfer functions of events 1 and 2 (Fig. 5b) is discussed later.

The model spectra are then obtained by the following equation:

$$S_{model}(\omega) = S_b(\omega) + \frac{T_{ave}(\omega)P(\omega)S_b(\omega)}{E_b(\omega)}. \quad (2)$$

This formula means that, given the mesoscale pressure spectrum P and local seiche spectrum S_b, we can model the observed meteotsunami spectrum, using the transfer function T.

3. Results

The observed spectra, background spectra, and model spectra are shown for 12 stations, in Figs. 6 and 7, for the first and second

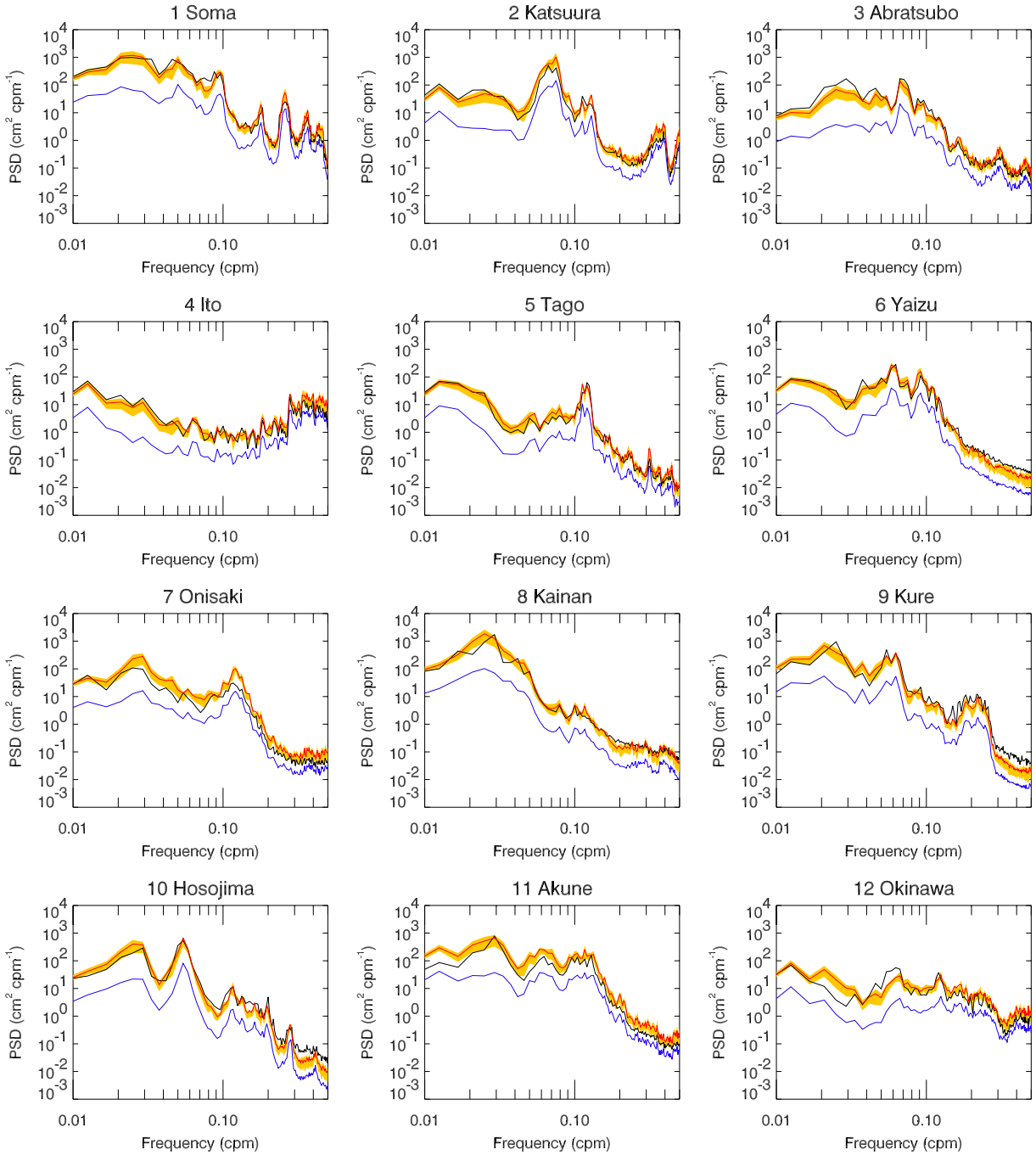

Fig. 7. Observed meteotsunami spectra (black), background seiche spectra (blue), and model spectra (red), with shaded area enclosing the upper and lower quartiles, of the second meteotsunami event for the 24-hour time interval from 2300 UT on 16 January 2022.

events, respectively. At all stations, the seiche eigenmodes are clear with a few peaks appearing in the background spectra. The outstanding eigenmodes for 12 stations are summarized in Supplement 2 Table A. Similar but amplified resonant features are evident in observed spectra and model spectra, suggesting the importance of "Abiki" for various different stations in Japan.

Further, it is also notable in Fig. 6 that even relatively weak eigenmodes are also enhanced at some stations. For example, the periodicity of ~9 min in Yaizu station and the periodicity of ~20 min at Kainan correspond to the discrete peaks in the pressure pulse spectrum (Fig. 5a).

As shown in Figs. 6 and 7, the observed and modeled spectra show good agreement over a wide frequency range, mostly within the expected 25−75% accuracy range (orange shaded region). The amplitude differences between observed and modeled spectra are within 50%. The worst agreement can be seen in Onisaki and Akune stations, where the coasts are differently facing parallel to the pressure-pulse wave front (Fig. 2).

4. Discussions

First, we discuss the scientific and societal impacts of this study. This study is useful as the first step to recognize the meteotsunami phenomenon which attracted great social attention in Japan. We showed the possibility that high time-cadence data of

barometric pressure can be utilized to model the meteotsunami amplitude, via the method of transfer function. The obtained results showed that the amplitude error of our model is smaller than 50%. Note, however, that the non-stationary character of both the pressure and tidal spectra was ignored in this study, and needs a separate study. The assumption of the spectral analysis was discussed in detail by Rabinovich (1997).

Second, we showed that the pressure spectra of P for only 4 hours gives a rough approximation of 24-hour meteotsunami trains. We interpret that this is reasonable because the Proudman effect, with a different longwave phase speed and the Lamb wave speed, can continuously disturb the downstream ocean in similar frequency with the pressure pulse as they propagate, keeping disturbed inlets to shelf and harbor for a long time of more than a day, although the physics-based simulation study must follow to validate this speculation.

Third, we cannot ignore tsunami propagating in the ocean for this event. The expected arrival timings of a tsunami to Japan's Pacific coast are 1430−1530 UT (midnight of Japan) on 15 January 2022. The tidal waveform basically did not basically change as it looked like enhanced eigenmodes, but the amplitude of tide disturbance peaked around the expected tsunami arrival time at many stations, as also seen in Fig. 3, which may indicate the possible influence to amplify the first meteotsunami by the following tsunami disturbance. That may also explain the different transfer function for the second pressure pulse event in which no later arrival of tsunami occurred. Note that the shape and value of the transfer function for event 1 are similar to the one obtained by Monserrat et al. (1998), peaking around 0.1 cpm, while the transfer function for event 2 does not have such a peak around 0.1 cpm and the amplitude at around 0.1 cpm is an order of magnitude smaller than that of event 1. Such an outstanding difference provide a hint for future simulation study to understand the basic characteristics of the seiche motions excited along the coast of Japan.

Finally, this study focused on Japan's local phenomena. However, to understand the ultimate cause and effects of meteotsunami events, and to obtain predictive physics-based time-domain model, it is essential to understand the global temporal and spatial evolution of the barometric pressure pulse itself that can drive meteotsunamis. The spatial structure of the Lamb waves changes according to the propagation from the eruption source and the interaction with the land and ocean. Further, as shown in this study, tsunami activity possibly changes the transfer function. Therefore, the properties of both Lamb and tsunami waves are important outputs of future simulation studies, and the air-sea coupled simulation results may be validated by checking if different transfer functions are obtained for the first and second meteotsunami events.

5. Conclusions

We examined the meteotsunami spectra for Tonga eruption event in January 2022. We highlighted the importance of localized resonance mechanism working at the last stage of multiple amplification steps, by showing that the seiche eigenmodes are enhanced at each station associated with the pressure pulses. The observed meteotsunamis can be characterized by the transfer function with an amplitude error within 50%, with the inputs of mesoscale pressure pulse spectra.

Acknowledgements

The tidal level data was provided by GSI, barometric pressure data was provided by Weathernews Inc., and Himawari-8 images and barometric pressure data of Chichijima Island were provided by JMA.

Edited by: K. Ito

Supplements

Supplement 1: Movie A. The color and cloud shading are based on band 8 which is infrared centered around 6.2 um, the Lamb wave is shown using time-derivative estimates on band 8, and smoothed using a Laplacian operator applied in longitude-latitude space.

Supplement 2: Table A. Outstanding periodicities of seiche eigenmodes at each station.

References

Harkrider, D., and F. Press, 1967: The Krakatoa air-sea waves: An example of pulse propagation in coupled systems. *Geophys. J. R. Astr. Soc.*, **13**, 149−159.

Hibiya, T., and K. Kajiura, 1982: Origin of the Abiki Phenomenon (a Kind of Seiche) in Nagasaki Bay. *J. Oceanogr. Soc. Japan*, **38**, 172−182.

Kulikov, E. A., A. B. Rabinovich, A. I. Spirin, S. L. Poole, and S. L. Soloviev, 1983: Measurement of tsunamis in the open ocean. *Mar. Geodesy*, **6**, 311−329.

Monserrat, S., A. B. Rabinovich, and B. Casas, 1998: On the reconstruction of the transfer function for atmospherically generated seiches. *Geophys. Res. Lett.*, **25**, 2197−2200.

Monserrat, S., I. Vilibic, and A. B. Rabinovich, 2006: Meteotsunamis: Atmospherically induced destructive ocean waves in the tsunami frequency band. *Nat. Hazards Earth Syst. Sci.*, **6**, 1035−1051.

Nishida, K., N. Kobayashi, and Y. Fukao, 2014: Background Lamb waves in the Earth's atmosphere. *Geophys. J. Int.*, **196**, 312−316, doi:10.1093/gji/ggt413.

Proudman, J., 1929: The effects on the Sea of changes in atmospheric pressure. *Geophys. Suppl. Mon. Notices R. Astro. Soc.*, **2**, 197−209.

Rabinovich, A. B., 1997: Spectral analysis of tsunami waves: Separation of source and topography effects. *J. Geophys. Res.*, **102**, 12663−12676.

Manuscript received 30 January 2022, accepted 4 April 2022
SOLA: *https://www.jstage.jst.go.jp/browse/sola/*